Original Research

Radek Fučík
Jiří Mikyška
Toshihiro Sakaki
Michal Beneš*
Tissa H. Illangasekare

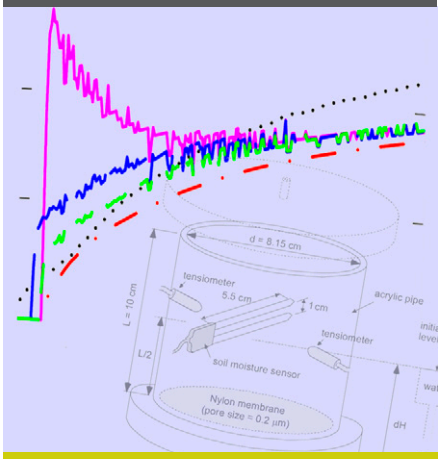

We studied the significance of the dynamic effect in capillarity in heterogeneous porous materials using numerical simulation of a laboratory experiment. The accumulation time of air at a material interface was investigated as a function of the ratio between air-entry pressure values of the adjacent sands.

R. Fučík, J. Mikyška, and M. Beneš, Dep. of Mathematics, Faculty of Nuclear Sciences and Physical Engineering, Czech Technical Univ., Trojanova 13, 120 00 Prague 2, Czech Republic; T. Sakaki and T.H. Illangasekare, Dep. of Environmental Science and Engineering, Colorado School of Mines, Golden, CO 80401-1843. *Corresponding author (michal.benes@fjfi.cvut.cz).

Vadose Zone J. 9:697–708
doi:09.0106/vzj2009.0106
Received 16 July 2009.
Published online 3 Aug. 2010.

Significance of Dynamic Effect in Capillarity during Drainage Experiments in Layered Porous Media

We developed one-dimensional, fully implicit numerical scheme to investigate the dynamic effect in the capillary pressure–saturation relationship used in the modeling of two-phase flow in porous media. Its validity was investigated by means of semianalytical solutions developed by McWhorter and Sunada (1990) and the authors. The numerical scheme was used to simulate a drainage experiment where the sand and fluid properties were known. Then the numerical scheme was used to simulate a laboratory experiment in a homogeneous column, including three major models of the dynamic effect coefficient τ. This numerical scheme can handle porous medium heterogeneity and was used to simulate a fictitious experimental setup with two different sands. As a result, the penetration time of the air phase through a layered porous medium for models including dynamic effects varied between 50 and 150% compared with static models of the capillary pressure–saturation relationship. Additionally, the accumulation time of air at a material interface (i.e., the delay of the air at the interface due to the capillary barrier effect) was investigated as a function of the ratio between the air-entry pressure values of the adjacent sands, emphasizing the differences between the dynamic and static capillary pressure models.

The prediction of flow of immiscible and incompressible fluids in porous media requires reliable models of capillary pressure–saturation relationships. In most past modeling efforts, various capillary pressure–saturation models were developed based on laboratory experiments where capillary pressure and saturation were measured under equilibrium conditions. Among these, the most commonly used are the models by Brooks and Corey (1964, p. 27) or van Genuchten (1980). The question has been raised, however, whether these static models accurately capture the dynamic behavior when the fluid phases are in motion. Alternative models based on both empirical and theoretical approaches have been proposed to deal with the dynamic effects associated with fluid flow. A method for these dynamic effects was proposed by Gray and Hassanizadeh (1991a,b), Hassanizadeh and Gray (1993), and Hassanizadeh et al. (2002). Our study analyzed the implications of the use of dynamic effects in the capillary pressure–saturation relationship in the modeling of water and air flow in homogeneous and heterogeneous porous media. We developed a numerical scheme to model these cases of dynamic flow. Subsequently, this numerical scheme was verified by comparing it with the semianalytical solutions for the static capillary pressure developed earlier for homogeneous cases (McWhorter and Sunada, 1990; Fučík et al., 2007) and for a layered system (Fučík et al., 2008). By means of experimental order of convergence criteria (eoc), we show that the developed numerical scheme is convergent and can be reliably used for simulating flow in both homogeneous and heterogeneous porous media systems.

The use of various models of dynamic effects in capillary pressure defined through an empirical coefficient (defined later as τ) was investigated and compared with the static model of capillary pressure. In unsaturated flow modeling, the two-phase flow system is simplified using the Richards equation, where the pressure of the nonwetting phase (air) is assumed to be constant throughout the flow domain. Using this simplification, as shown in Ippisch et al. (2006), the dynamic effect was not found to be of importance for the heterogeneous system that was studied. Other numerical studies on the dynamic effect in capillary pressure models have been reported (Manthey et al., 2005; Manthey, 2006; Peszyńska and Yi, 2008); however, the implications of using the dynamic capillary pressure models in two-phase models (without the assumption of constant nonwetting phase pressure) have not been fully

investigated. Helmig et al. (2007) presented a semi-implicit numerical scheme based on the upwind finite volume method, where the material interfaces in a heterogeneous system are handled using the Lagrange multiplier method. In a subsequent study (Helmig et al., 2009), the idea was further developed. In those studies, only a constant dynamic effect coefficient was considered. Another interesting tool for studying dynamic effects in capillarity was presented in van Duijn et al. (2007), where traveling wave solutions were considered for two-phase flow involving a simplified model for dynamic effects in capillarity. This method is not applicable, however, when the constitutive models are nonlinear, as in the case of two-phase flow.

In past studies, the dynamic effect coefficient was assumed to depend on water saturation (Sakaki et al., 2010; O'Carroll et al., 2005; Nieber et al., 2005), which was also supported by experimental data generated in our group. We believe that this is critical, especially in heterogeneous porous media. The fully implicit numerical scheme that we developed can be used for a detailed investigation of the saturation and capillary pressure behavior when a dynamic effect in capillary pressure is used in modeling two-phase flow. De Neef and Molenaar (1997) presented a method to describe the nonwetting phase flow behavior at material interfaces using static capillary pressures and we extended this approach for the dynamic effect. The developed numerical scheme was used to investigate the behavior of different functional models of the dynamic capillary pressure coefficient in drainage flow regimes.

Mathematical Model

In this study, two phases—a wetting phase (indexed *w*) and a nonwetting phase (indexed *n*)—were considered to be present within the pores of a porous medium and both fluids were assumed to be incompressible and immiscible. Under these assumptions, the following one-dimensional $p_w - S_n$ formulation (Bastian, 1999) in a domain $\Omega = [0,L]$ is given by

$$\Phi \frac{\partial S_\alpha}{\partial t} + \frac{\partial u_\alpha}{\partial x} = 0 \qquad [1]$$

$$u_\alpha = -\frac{k_{r\alpha}}{\mu_\alpha} K \left[\frac{\partial}{\partial x} \left(p_w + \delta_{\alpha n} p_c \right) - \rho_\alpha g \right] \qquad [2]$$

where $S_w + S_n = 1$; $\delta_{\alpha n}$ is the Kronecker symbol; $\alpha = w, n$; S_α is the saturation, p_α the pressure, ρ_α the volumetric density, μ_α the dynamic viscosity, and $k_{r\alpha}$ the relative permeability of the α phase; the Darcy velocities are denoted by u_α; and Φ, K, and g stand for the porosity, the permeability of the soil matrix, and the gravitational acceleration, respectively. A summary of the symbols used here, including units, is given in the Appendix.

The governing Eq. [1] and [2] are subjected to an initial condition

$$S_\alpha = S_\alpha^0 \quad \text{in } \Omega \qquad [3]$$

and boundary conditions

$$\begin{aligned} u_\alpha \cdot \mathbf{n} &= u_\alpha^N, \quad \text{on } \Gamma_{u_\alpha}^N \\ S_\alpha &= S_\alpha^D, \quad \text{on } \Gamma_S^D \\ p_\alpha &= p_\alpha^D, \quad \text{on } \Gamma_{p_\alpha}^D \end{aligned} \qquad [4]$$

where $\mathbf{n}$ denotes the outer normal vector to the boundary. Generally, $\Gamma_{u_\alpha}^N$, Γ_S^D, and $\Gamma_{p_\alpha}^D$ denote subsets of the boundary Γ of the domain Ω, here, $\Gamma = \{0,L\}$, with Γ^D denoting a Dirichlet-type boundary subset and Γ^N a Neumann-type boundary subset.

Following the standard definitions in the literature (Bear and Verruijt, 1990; Helmig, 1997), the capillary pressure p_c at the pore scale is defined as the difference between the nonwetting-phase pressure p_n and the wetting-phase pressure p_w:

$$p_c = p_n - p_w \qquad [5]$$

At the macro scale, the capillary pressure has been commonly considered to be a function of the wetting-phase saturation only (Helmig, 1997; Bear and Verruijt, 1990; Mikyška et al., 2009; Fučík et al., 2004, 2005, 2007). In this study, this assumption was justified because we considered only drainage flow regimes without hysteresis. We used the following Brooks and Corey (1964, p. 27) model of the capillary pressure–saturation relationship in the two-phase flow model:

$$p_c^{eq} = p_d \left(S_w^e \right)^{-1/\lambda} \qquad [6]$$

where p_d is the entry pressure, λ is the pore size distribution index, and S_w^e is the effective saturation of the wetting phase, defined as

$$S_\alpha^e = \frac{S_\alpha - S_{r\alpha}}{1 - S_{rw} - S_{rn}} \qquad [7]$$

where $S_{r\alpha}$ is the α-phase irreducible saturation. A superscript eq is used in Eq. [6] with respect to p_c and it indicates the model of the capillary pressure for the system in a state of thermodynamic equilibrium.

The Brooks and Corey relationship (Eq. [6]) is suitable for modeling flow in heterogeneous porous media because the difference in the entry pressure coefficients p_d in different porous materials captures the barrier effect that has been observed in various experiments (Illangasekare et al., 1995). The permeability model according to Burdine (1953) and Brooks and Corey (1964, p. 27) is given as

$$\begin{aligned} k_{rw} &= \left(S_w^e \right)^{3+2/\lambda} \\ k_{rn} &= \left(1 - S_w^e \right)^2 \left[1 - \left(S_w^e \right)^{1+2/\lambda} \right] \end{aligned} \qquad [8]$$

The dynamic capillary pressure–saturation relationship has been proposed in the following form (Gray and Hassanizadeh, 1991b)

Table 1. Properties of porous media and fluids used in the numerical simulation and experimentally determined models of the dynamic effect coefficient τ (Eq. [9]) for Sand A and fictitious calculated values of τ for Sands B and C.

Sand property	Sand A	Sand B	Sand C
CESEP† labels	Ohji sand (field sand)	Sand no. 70 (silica sand)	Sand no. 110 (silica sand)
Porosity (Φ)	0.448	0.418	0.343
Intrinsic permeability (K), m^2	1.63×10^{-11}	1.44×10^{-11}	5.168×10^{-12}
Residual water saturation (S_{wr})	0.265	0.089	0.040
Entry pressure (p_d), Pa	3450	4042	8028
Pore size distribution index (λ)	4.66	5.32	5.41
Models of τ, Pa s			
Stauffer model τ_S	$\tau_{S,A} = 3.3 \times 10^5$	$\tau_{S,B} = 4.85 \times 10^5$	$\tau_{S,C} = 4.25 \times 10^6$
Constant model τ_{const}	$\tau_{const,A} = 1.1 \times 10^6$	$\tau_{const,B} = (\tau_{S,B}/\tau_{S,A})\tau_{const,A}$	$\tau_{const,C} = (\tau_{S,C}/\tau_{S,A})\tau_{const,A}$
Linear model τ_{lin}	$\tau_{lin,A}(S_w) = 3.2 \times 10^6(1 - S_w)$	$\tau_{lin,B} = (\tau_{S,B}/\tau_{S,A})\tau_{lin,A}$	$\tau_{lin,C} = (\tau_{S,C}/\tau_{S,A})\ \tau_{lin,A}$
Loglinear model τ_{log}	$\tau_{log,A}(S_w) = 10^8\exp(-7.7S_w)$	$\tau_{log,B} = (\tau_{S,B}/\tau_{S,A})\tau_{log,A}$	$\tau_{log,C} = (\tau_{S,C}/\tau_{S,A})\tau_{log,A}$
Fluid property	**Water**	**Air**	
Density (ρ), kg m^{-3}	997.8	1.205	
Dynamic viscosity (μ), kg m^{-1} s^{-1}	9.77×10^{-4}	1.82×10^{-5}	

† Labels used by the Center for Experimental Study of Subsurface Environmental Processes, Colorado School of Mines, Golden.

$$p_c := p_n - p_w = p_c^{eq} - \tau\frac{\partial S_w}{\partial t} \qquad [9]$$

where p_c^{eq} is the capillary pressure–saturation relationship in thermodynamic equilibrium of the system and τ, the dynamic effect coefficient, is a material property of the system.

In 1978, before the thermodynamic definition of capillary pressure (Eq. [9]) in Gray and Hassanizadeh (1991b), Stauffer (1978) observed the dynamic effect in laboratory experiments and proposed the following empirical expression for τ:

$$\tau_S = \alpha_S \frac{\mu_w \Phi}{K\lambda}\left(\frac{p_d}{\rho_w g}\right)^2 \qquad [10]$$

where $\alpha_S = 0.1$ denotes a scaling parameter. Both λ and p_d are the Brooks and Corey parameters that can be experimentally determined.

The Stauffer model for the dynamic effect coefficient τ_S was obtained by correlating experimental data. The values of τ_S vary between 2.4×10^4 and 7.7×10^4 Pa s (Manthey, 2006, p. 27). In the case of the sands used in this study (see Table 1), Eq. [10] gives higher values of τ_S than for the sands used by Stauffer (1978). Other researchers have suggested that the magnitude of τ should be smaller, i.e., on the order of 10^2 to 10^3 Pa s (Dahle et al., 2005), or, on the other hand, it should be higher, i.e., on the order of 10^4 to 10^8 Pa s (Hassanizadeh et al., 2002). Furthermore, the dynamic coefficient may depend on averaging scales as well as saturation (Nordbotten et al., 2007, 2008). As the influence of the averaging scales was not found to be important in Camps-Roach et al. (2010), we did not consider that dependence in this study.

In this study, we considered τ as a function of S_w and we used experimentally determined functional models of $\tau(S_w)$ in the numerical simulations to investigate their influence on two-phase flow simulations. The laboratory experiment is described briefly below and in detail in Sakaki et al. (2010).

Material Interface

In this section, we extend the approach of de Neef and Molenaar (1997) to the case of dynamic capillary pressure conditions.

Let us consider an initially fully water-saturated column with two sands separated by a sharp interface. The situation at the interface is illustrated in Fig. 1. The Brooks and Corey capillary pressure curves (Eq. [6]) for the sands used in this study are shown in Fig. 2. As the nonwetting phase reaches the material interface from the coarse sand (denoted by the superscript I), the interfacial capillary pressure p_c^I increases. When p_c^I is lower than the entry pressure p_d^{II} of the finer medium, the nonwetting phase cannot penetrate the interface (i.e., its flux through the interface is zero) and starts to accumulate at the interface. Once the capillary pressure p_c^I exceeds the entry pressure threshold p_d^{II}, the nonwetting phase enters the finer sand.

Altogether, the condition at the material interface is established in the following form:

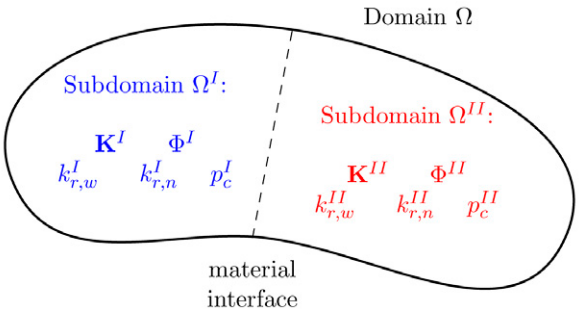

Fig. 1. Illustration of the situation at the interface between two porous subdomains, Ω^{I} and Ω^{II}, where the material properties of intrinsic permeability (K), porosity (Φ), relative permeability of the wetting and nonwetting phases ($k_{\mathrm{r,w}}$ and $k_{\mathrm{r,n}}$, respectively), and capillary pressure (p_{c}) can be discontinuous.

$$\begin{aligned} &S_{\mathrm{n}}^{\mathrm{II}} = 0 \text{ and } p_{\mathrm{c}}^{\mathrm{II}} = p_{\mathrm{d}}^{\mathrm{II}} \quad \text{if } p_{\mathrm{c}}^{\mathrm{I}} < p_{\mathrm{d}}^{\mathrm{II}} \\ &p_{\mathrm{c}}^{\mathrm{I}} = p_{\mathrm{c}}^{\mathrm{II}} \quad \text{otherwise} \end{aligned} \tag{11}$$

Equation [11] is referred to as the *extended capillary pressure condition* (van Duijn et al., 1995; de Neef and Molenaar, 1997). In the case of static capillary pressure, a unique value of the wetting phase saturation $S_{\mathrm{w}}^{*,\mathrm{I}}$ can be associated with the threshold value of the capillary pressure such that

$$S_{\mathrm{w}}^{*,\mathrm{I}} = \left(p_{\mathrm{c}}^{\mathrm{I}}\right)^{-1}\left(p_{\mathrm{d}}^{\mathrm{II}}\right) \tag{12}$$

as shown in Fig. 2.

We assumed that the condition in Eq. [11] also holds for the dynamic capillary pressure in the form

$$\begin{aligned} &S_{\mathrm{n}}^{\mathrm{II}} = 0 \text{ and } p_{\mathrm{c}}^{\mathrm{II}} = p_{\mathrm{d}}^{\mathrm{II}} && \text{if } p_{\mathrm{c}}^{\mathrm{I}} < p_{\mathrm{d}}^{\mathrm{II}} \\ &p_{\mathrm{c}}^{\mathrm{eq,I}} - \tau^{\mathrm{I}}\frac{\partial S_{\mathrm{w}}^{\mathrm{I}}}{\partial t} = p_{\mathrm{c}}^{\mathrm{eq,II}} - \tau^{\mathrm{II}}\frac{\partial S_{\mathrm{w}}^{\mathrm{II}}}{\partial t} && \text{otherwise} \end{aligned} \tag{13}$$

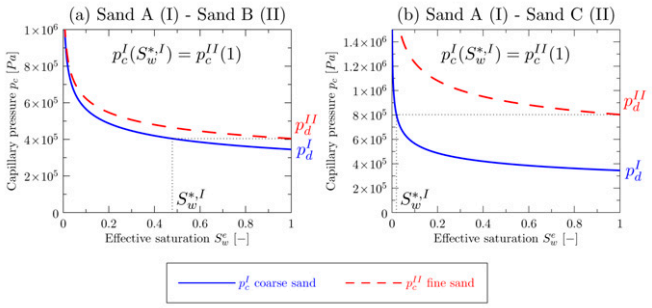

Fig. 2. Curves of the static capillary pressure models for coarse over fine sand configurations: (a) Sand A over Sand B and (b) Sand A over Sand C. The threshold value $S_{\mathrm{w}}^{*,\mathrm{I}}$ is the value where the capillary pressure $p_{\mathrm{c}}^{\mathrm{I}}$ of the coarser sand is equal to the entry pressure $p_{\mathrm{d}}^{\mathrm{II}}$ of the finer sand.

In contrast to the static capillary pressure model, the threshold saturation cannot be uniquely associated with the entry pressure of the finer sand as in Eq. [12] because the value of the dynamic capillary pressure depends on the dynamics of the system through the time derivative of the saturation. Consequently, the required entry pressure threshold p_{d} can be reached for higher values of $S_{\mathrm{w}}^{\mathrm{I}}$ than in the static case.

Numerical Model

We used a standard, finite-volume, discretization technique to determine the approximate discrete solutions $S_{\mathrm{n},i}^{k} = S_{\mathrm{n}}(k\Delta t, i\Delta x)$ and $p_{\mathrm{w}}(k\Delta t, i\Delta x)$ of the problem (Eq. [1]), where $i = 0, 1, \ldots, M$, $M\Delta x = L$, $k = 0, 1, \ldots, N$, and $N\Delta t = T$, where L denotes the length of the domain and T is the final time of the simulation. Within this standard numerical scheme, we propose a new scheme to treat the material interfaces.

The fully implicit numerical scheme is given as

$$\Phi\frac{S_{\alpha,i}^{k+1} - S_{\alpha,i}^{k}}{\Delta t} = -\frac{u_{\alpha,i+1/2}^{k+1} - u_{\alpha,i-1/2}^{k+1}}{\Delta x} \tag{14}$$

where $\alpha = w, n$. The discrete Darcy velocities u_{α} introduced by Eq. [2] are given by

$$u_{\alpha,i+1/2}^{k+1} = -\frac{K}{\mu_{\alpha}}k_{\mathrm{r}\alpha}\left(S_{\alpha,\mathrm{upw}}^{k+1}\right) \underbrace{\left(\frac{p_{\mathrm{w},i+1}^{k+1} - p_{\mathrm{w},i}^{k+1}}{\Delta x} + \delta_{\alpha\mathrm{n}}\frac{p_{\mathrm{c},i+1}^{k+1} - p_{\mathrm{c},i}^{k+1}}{\Delta x} - \rho_{\alpha}g\right)}_{\left(\partial\Psi/\partial x\right)^{i+1/2}} \tag{15}$$

and the discrete capillary pressure by

$$\begin{aligned} p_{\mathrm{c},i}^{k+1} &= p_{\mathrm{c}}\left(1 - S_{\mathrm{n},i}^{k+1}, -\frac{S_{\mathrm{n},i}^{k+1} - S_{\mathrm{n},i}^{k}}{\Delta t}\right) \\ &= p_{\mathrm{c}}^{\mathrm{eq}}\left(1 - S_{\mathrm{n},i}^{k+1}\right) + \tau\left(1 - S_{\mathrm{n},i}^{k+1}\right)\frac{S_{\mathrm{n},i}^{k+1} - S_{\mathrm{n},i}^{k}}{\Delta t} \end{aligned} \tag{16}$$

where $S_{\alpha,\mathrm{upw}}^{k+1}$ is the saturation taken in the upstream direction with respect to the gradient of the phase potential Ψ_{α}, i.e.,

$$S_{\alpha,\mathrm{upw}}^{k+1} = \begin{cases} S_{\alpha,i+1}^{k+1} & \text{if } \left(\partial\Psi/\partial x\right)^{i+1/2} \geq 0 \\ S_{\alpha,i}^{k+1} & \text{if } \left(\partial\Psi/\partial x\right)^{i+1/2} < 0 \end{cases} \tag{17}$$

The fully implicit numerical scheme is solved using the Newton–Raphson iteration method in which the Jacobi matrix is block tridiagonal. In each iteration, a new guess of discrete saturation $S_{\mathrm{n},i}^{k+1}$ is given (in the current time step $k + 1$) and the upstream saturations in Eq. [15] are recomputed.

At the material interface, the extended capillary pressure condition (Eq. [13]) implies a jump in saturation (see Fig. 2). Such discontinuous saturation is represented by $S_{n,i}^{I}$ and $S_{n,i}^{II}$ (see Fig. 3), where i is the index of the node located at the material interface. At this node, the discrete saturation in the Newton–Raphson iteration process $S_{n,i}^{k+1}$ corresponds to the saturation of the porous medium with lower entry pressure, i.e., here $S_{n,i}^{k+1} = S_{n,i}^{I,k+1}$. The other interfacial saturation $S_{n,i}^{II,k+1}$ is determined using the extended capillary pressure condition Eq. [11]:

$$S_{n,i}^{II,k+1} = \begin{cases} 0 & \text{if } p_{c,i}^{I,k+1} < p_d^{II} \\ \text{solution of } p_{c,i}^{I,k+1} = p_{c,i}^{II,k+1} & \text{otherwise} \end{cases} \quad [18]$$

where the discrete capillary pressures are given by Eq. [16].

An analysis of the second option in Eq. [18] reveals that $S_{n,i}^{II,k+1}$ is the solution of

$$p_c^{eq,I}\left(1-S_{n,i}^{I,k+1}\right)+\tau^{I}\left(1-S_{n,i}^{I,k+1}\right)\frac{S_{n,i}^{I,k+1}-S_{n,i}^{I,k}}{\Delta t} = p_c^{eq,II}\left(1-S_{n,i}^{II,k+1}\right)+\tau^{II}\left(1-S_{n,i}^{II,k+1}\right)\frac{S_{n,i}^{II,k+1}-S_{n,i}^{II,k}}{\Delta t} \quad [19]$$

Equation [19] is a nonlinear equation that couples $S_{n,i}^{I,k+1}$ and $S_{n,i}^{II,k+1}$. In Eq. [19], the interfacial saturations from the previous time step $S_{n,i}^{I,k}$ and $S_{n,i}^{II,k}$ are also required. Therefore, using only one interfacial saturation to store values from the previous time steps would give rise to a numerically expensive recursion. Hence, an extra variable is added into each interfacial node to store both interfacial saturations $S_{n,i}^{I}$ and $S_{n,i}^{II}$ from the previous time step.

Verification of the Numerical Scheme

The numerical scheme (Eq. [14–19]) was benchmarked by semianalytical solutions that were available only for the static capillary pressure model and no gravity, i.e., $\tau = 0$ and $g = 0$. The reliability of the numerical scheme was determined for a homogeneous and a heterogeneous porous medium. The experimental order of convergence eoc_k estimates the theoretical order of convergence of a numerical scheme and is computed using the L_k norm of the difference between the numerical S_n^{num} and the semianalytical S_n^{an} solutions at the final time of the simulation, where we used $k = 1,2$. The L_k norm of an integrable function f raised to the power k is given as

$$\|f\|_k = \left(\int_0^L |f(x)|^k \mathrm{d}x\right)^{1/k} \quad [20]$$

For numerical solutions on two meshes with mesh sizes Δx_1 and Δx_2, denoted as $S_{n,\Delta x_1}^{num}$ and $S_{n,\Delta x_2}^{num}$, respectively, we expect their errors in the form

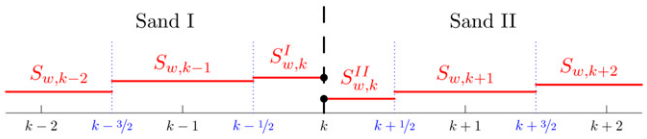

Fig. 3. Discretization of the saturation S_w by the vertex-centered finite volume method. The saturation jump at material discontinuity (in node k) is handled using two discrete values, $S_{w,k}^{I}$ and $S_{w,k}^{II}$.

$$\left\|S_{n,\Delta x_1}^{num}-S_n^{an}\right\|_k = C\left(\Delta x_1\right)^{\varepsilon}$$
$$\left\|S_{n,\Delta x_2}^{num}-S_n^{an}\right\|_k = C\left(\Delta x_2\right)^{\varepsilon} \quad [21]$$

where C is some positive constant and ε is the order of convergence of the numerical scheme. Using Eq. [21], ε is approximated by eoc_k as

$$\varepsilon \approx \mathrm{eoc}_k\left(\Delta x_1, \Delta x_2\right) = \frac{\ln\left\|S_{n,\Delta x_1}^{num}-S_n^{an}\right\|_k - \ln\left\|S_{n,\Delta x_2}^{num}-S_n^{an}\right\|_k}{\ln \Delta x_1 - \ln \Delta x_2} \quad [22]$$

First, we investigated two-phase flow of air and water in a horizontal one-dimensional column filled with a homogeneous sand. Water was displaced by air due to the imposed flux of air at the boundary. In this case, the flow is governed by both capillarity and advection. As the domain is placed horizontally, i.e., $g = 0$, the generalized McWhorter problem formulation in Fučík et al. (2007) can be used to obtain a semianalytical solution. The description of the model parameters and initial and boundary conditions are given in Table 2. The resulting air saturation S_n and capillary pressure p_c compared with the McWhorter and Sunada (1990) semianalytical solution are shown in Fig. 4a and the values of eoc show the convergence rate of the numerical solution toward the exact solution in Table 3. These values of eoc in Table 3 are typical for a first-order numerical scheme with upwind technique (LeVeque, 2002).

In the case of a porous medium with a single material discontinuity, we verified the implementation of the interfacial condition

Table 2. Parameters of the McWhorter and Sunada (1990) benchmark problem in a homogeneous porous medium.

Parameter	Value
Initial condition	$S_n(x,0) = 0$ for x in $(0,L)$
Boundary conditions	$S_n(0,t) = 0.73$ for t in $[0,T]$
	$S_n(L,t) = 0$ for t in $[0,T]$
	$u_n(0,t) = u_0(t) = 1.63 \times 10^{-3} t^{-1/2}$ for t in $[0,T]$
	$u_w(L,t) = 0.9u_0(t)$ for t in $[0,T]$
Problem setup	$T = 1000$ s, $L = 1$ m, $g = 0$
Capillary pressure	Static model (Eq. [6]), $p_c \equiv p_c^{eq}$, $\tau = 0$
Material	Sand A, Table 1
Fluids	Air and water, Table 1

Table 3. Experimental orders of convergence (eoc) of the numerical scheme for homogeneous and layered (heterogeneous) porous media measured in L_1 and L_2 norms (Eq. [20]), respectively. The convergence of the numerical scheme toward the analytical solution for both homogeneous and heterogeneous cases is illustrated in Fig. 4.

Mesh size	eoc_1	eoc_2
cm		
Homogeneous medium		
4 → 2	0 83	0.64
2 → 1	0.73	0.64
1 → 1/2	0.75	0.65
1/2 → 1/4	0.77	0.67
1/4 → 1/8	0.79	0.68
1/8 → 1/16	0.81	0.70
Heterogeneous medium		
1 → 1/2	0.71	0.45
1/2 → 1/4	0.84	0.52
1/4 → 1/8	0.96	0.58
1/8 → 1/16	1.03	0.65
1/16 → 1/32	1.03	0.75
1/32 → 1/64	1.07	0.96

(Eq. [19]) using the semianalytical solution developed in Fučík et al. (2008). We considered a porous medium consisting of two homogeneous blocks separated by a sharp interface. The system of Eq. [1] can be reformulated into the problem published in van Duijn and de Neef (1996), where the material discontinuity is located in the middle of the domain at $L/2$. In Fučík et al. (2008), we generalized the van Duijn and de Neef problem formulation to include both advection and capillarity. The resulting problem formulation requires that the initial saturation distribution and the boundary fluxes are prescribed as shown in Table 4. In Fig. 4b, the numerical solutions are compared with the semianalytical solution and the experimental order of convergence is shown in Table 3. As in the previous case, the values of the eoc show a convergence rate of the numerical solution toward the semianalytical solution.

As shown in Fig. 4b, the jump in saturations across the interface in the case of the heterogeneous porous medium was determined correctly. The estimated experimental orders of convergence (eocs) indicate that the numerical solution converges to the analytical solution in both homogeneous and heterogeneous benchmarks. In the following discussion, this is used as a referential solution for further investigation of the interfacial condition Eq. [13] in heterogeneous porous media. A more detailed numerical analysis of the scheme can be found in Fučík et al. (2009).

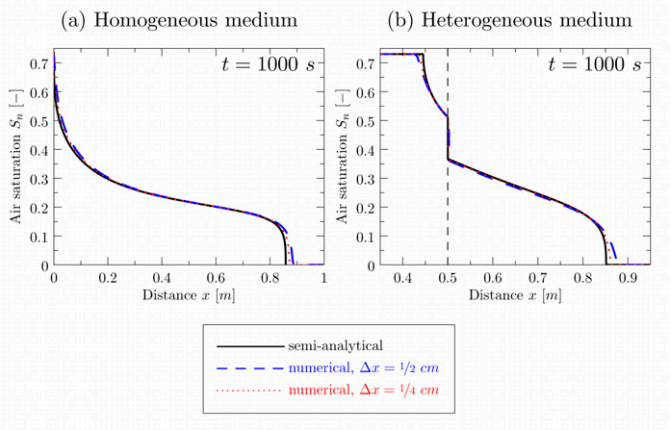

Fig. 4. Numerical solution of the McWhorter and Sunada problem in (a) homogeneous and (b) heterogeneous porous media placed horizontally; time t = 1000 s, and $\Delta t/(\Delta x)^2 = 4$ s cm^{-2} is kept constant. Illustration of the convergence of the numerical solutions toward the semianalytical solution (drawn as a solid line). The corresponding experimental orders of convergence are given in Table 3.

Numerical Experiments

We used the numerical scheme (Eq. [14–19]) to simulate two problems of two-phase flow in a homogeneous and a heterogeneous porous medium. In both situations, immiscible and incompressible displacement of water by air was considered.

Simulation 1: Numerical Simulation of a Laboratory Experiment

The first problem simulated a laboratory experiment that was performed in the Center for Experimental Study of Subsurface Environmental Processes, Colorado School of Mines. As a result of this experiment, three functional models of the dynamic effect coefficient $\tau = \tau(S_w)$ were correlated (Sakaki et al., 2010).

The experiment in Fig. 5 consisted of a single, vertically placed, 10-cm-long Tempe cell uniformly filled with a homogeneous field sand from the Ohji site sampled in Tokyo, Japan. This sand is denoted as Sand A (see Table 1). Initially, the column was flushed with water such that no air phase was present inside, as shown in Fig. 6, Case 1. A series of slow drainage steps was performed to determine the capillary pressure–saturation relationship in equilibrium p_c^{eq}. The measured Brooks and Corey model parameters are shown in Table 1. Then, a series of fast primary drainage experiments was performed and values of the capillary pressure and the air saturation were measured every 15 s by sensors in the middle of the column. The values of τ were directly calculated using Eq. [9] and the model of the static capillary pressure p_c^{eq} that was measured separately using the same soil sample. In the primary drainage cycle, the measured τ exhibited a dependency on saturation as in Fig. 7; thus, three models were fitted and evaluated. These are given in Table 1.

Table 4. Parameters of the advection and capillary diffusion benchmark problem in a heterogeneous porous medium.

Parameter	Value
Initial condition	$S_n(x,0) = 0.73$ for x in $(0,L/2)$
	$S_n(x,0) = 0$ for x in $(L/2,L)$
Boundary conditions	$S_n(0,t) = 0.73$ for t in $[0,T]$
	$S_n(L,t) = 0$ for t in $[0,T]$
	$p_n(0,t) =$ constant $= 0$ for t in $[0,t]$
	$u_w(L,t) + u_n(L,t) = 1.59 \times 10^{-3} t^{-1/2}$ for t in $[0,T]$
Problem setup	$T = 1000$ s, $L = 2$ m, $g = 0$
Capillary pressure	
	Static model (Eq. [6]), $p_c \equiv p_c^{eq}$, $\tau = 0$
Materials	Sand A (coarse), Table 1 in $(0,L/2)$
	Sand B (fine), Table 1 in $(L/2,0)$
Fluids	Air and water, Table 1

We simulated the experiment as a one-dimensional problem with different models of $\tau(S_w)$. The parameters of the discrete problem (Eq. [14–16]) are summarized in Table 5.

In these numerical simulations, the measured outflow of water (denoted as u_{water} and shown as the solid line in Fig. 8) was used as a Neumann boundary condition at the bottom of the column ($x = L$). The resulting temporal profiles of the air saturation S_n and the capillary pressure p_c are shown in Fig. 9a.

The nonsmooth shapes of the numerical solutions in Fig. 9a were caused solely by the nonsmoothness of the prescribed flux of water. Because the temporal derivative of the air saturation is directly influenced by the given flux, the nonsmoothness is magnified in the values of the dynamic capillary pressure given by Eq. [9]. That is why the bumps do not appear in the case of the static capillary pressure.

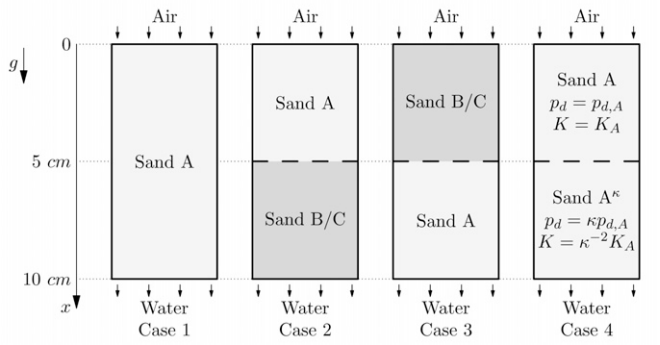

Fig. 6. Sketch of homogeneous (Case 1) and layered (Cases 2–4) configurations of the porous medium. In each case, the porous medium was placed vertically and fully water saturated, $S_w = 1$, at time $t = 0$ s. The gravitational acceleration vector g points in the positive x direction. Sands A and A$^\kappa$ differ only in the ratio between the entry pressures. The entry pressure and the intrinsic permeability of Sand A$^\kappa$ is $p_d = \kappa p_{d,A}$ and $K = \kappa^{-2} K_A$, respectively, where $p_{d,A}$ is the entry pressure and K_A is the intrinsic permeability of Sand A.

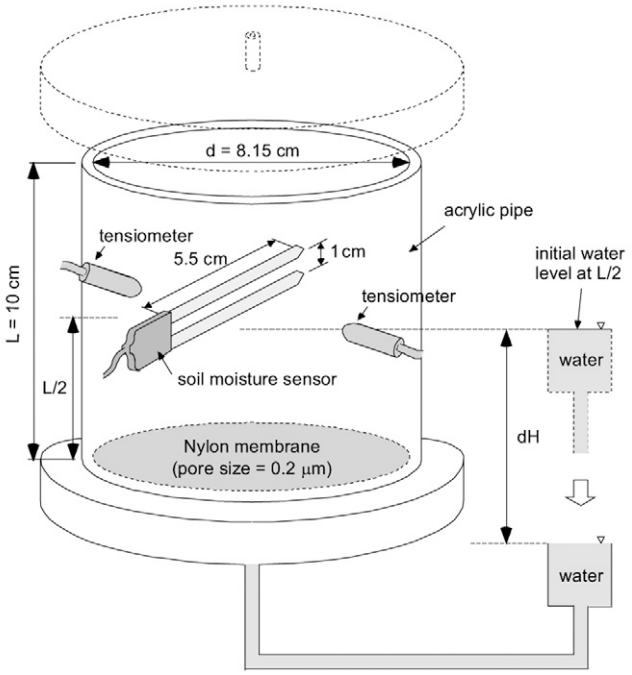

Fig. 5. Schematic view of the experimental setup. The upper part was exposed to the atmosphere through a small hole in the top cap. The lower part was connected to a constant-head water reservoir. The water pressure was measured with two tensiometers and averaged (from Sakaki et al., 2010).

To assure that the differences among the numerical solutions with respect to different models of $\tau(S_w)$ were not caused by the nonsmoothness of the prescribed flux, we used a smooth functional approximation of the boundary flux that preserves the total mass of the effluent water in the form

$$u^*_{water}(t) = 3.7\times10^{-5} \exp(-1.7\times10^{-3} t) + 7.4\times10^{-7} \text{ m s}^{-1} \quad [23]$$

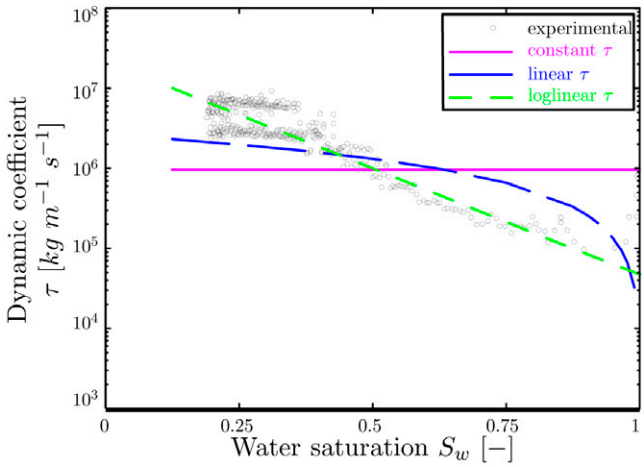

Fig. 7. Fitted models of the dynamic coefficient τ (logarithmic scale) to the observed laboratory data (from Sakaki et al., 2010).

Table 5. Parameters of the simulation of the laboratory experiment (Simulation 1). The profiles of the measured and smoothly approximated flux of water, u_{water} and u^*_{water}, respectively, are shown in Fig. 8.

Parameter	Value
Initial condition	$S_n(x,0) = 0$ for x in $(0,L)$
Boundary conditions	$u_w(0,t) = 0$ for t in $[0,T]$
	$p_n(0,t) =$ constant $= 0$ for t in $[0,T]$
	$u_w(L,t) = u_{water}(t)$ or $u_{water}{}^*(t)$ for t in $[0,T]$
	$u_n(L,t) = 0$ for t in $[0,T]$
Problem setup	$T = 5000$ s, $L = 10$ cm, $g = 9.81$ m s^{-2}
Capillary pressure	Dynamic capillary pressure p_c, various models for $\tau(S_w)$, Table 1
Material	Sand A, Table 1
Fluids	Air and water, Table 1

In Fig. 8, the measured flux of water is compared with its smooth functional approximation u^*_{water}. As shown in Fig. 9b, the numerical solutions using the flux u^*_{water} are smooth alternates to the bumpy-shaped solutions in Fig. 9a. Consequently, the bumpiness of the capillary pressure was not caused by the numerical scheme, and the nonsmoothness of the prescribed flux did not significantly affect the overall temporal profiles of the solutions.

The influence of different models of the dynamic effect coefficient τ on the numerical solution of the air saturation S_n was negligible (see Fig. 9a). On the other hand, their influence on the capillary pressure p_c is important in cases where there is a temporal change in the saturation S_n because the temporal derivative of S_n is multiplied by the dynamic effect coefficient τ in Eq. [9]. The constant model for τ does not seem to be a good model for the appropriate approximation because it overestimated the laboratory-measured dynamic coefficient for high wetting-phase saturation (see Fig. 7) and its numerical solution of p_c differed substantially from the measured capillary pressure (see Fig. 9a).

Simulation 2: Numerical Simulation in a Heterogeneous Porous Medium

We investigated the effects of different dynamic capillary pressure models on the behavior of the nonwetting phase at heterogeneity interfaces. Because no laboratory experiment involving dynamic capillary pressure was available for the case of a heterogeneous porous medium, only a numerical simulation is provided here. Similar to the setup of the laboratory experiment in Simulation 1, we considered a vertically placed column filled with two different sands, where we combined Sand A and a finer Sand B or C. These sands were separated by a sharp interface in the middle of the column, as shown in Fig. 6, Cases 2 and 3. Initially, the column was fully water saturated. At $t = 0$, the water started to flow out of the column at $x = L$ with a flow rate given by Eq. [23]. The model parameters are summarized in Table 6.

Unfortunately, there is no known laboratory-measured model for the dynamic coefficient τ for Sand B or C and the air–water system; however, the Stauffer model $\tau_{S,B}$ and $\tau_{S,C}$, respectively, can be computed for these sands. Based on the ratio between the Stauffer model $\tau_{S,A}$ for Sand A and $\tau_{S,B}$ or $\tau_{S,C}$, the three functional relationships $\tau = \tau(S_w)$ were estimated from the laboratory-determined Sand A models as shown in Table 1.

In Fig. 10, we show the position of the air front with time for different models of the dynamic coefficient $\tau = \tau(S_w)$. First, the air flowed from the coarse to the fine sand (Fig. 10a and 10b), where the barrier effect was simulated. The barrier effect, modeled by the Brooks and Corey model (Eq. [6]) and the extended capillary pressure condition (Eq. [11]) for the capillary pressure p_c, implies that the nonwetting fluid (air) cannot enter the finer sand unless its capillary pressure at the interface is higher than the entry pressure p_d of the finer sand (Helmig, 1997; Brooks and Corey, 1964, p. 27). We then considered the opposite configuration (Fig. 10c and 10d), where the barrier effect did not occur. In all cases, the use of the linear model of $\tau = \tau(S_w)$ caused faster propagation of the air front in the homogeneous layers of the porous medium, whereas the log-linear model did not influence the speed substantially with respect to the use of the

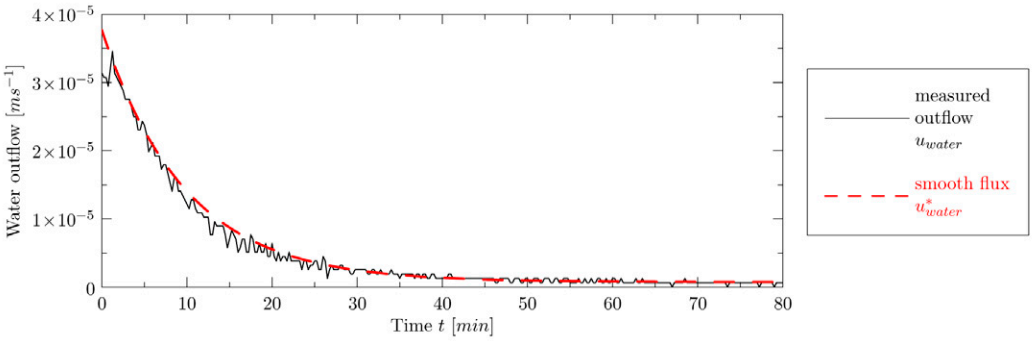

Fig. 8. Measured (solid line) and smoothly approximated (dashed line) water outflow from the bottom of the column (at $x = 10$ cm). We used the smooth approximation to demonstrate that the numerical scheme works for both non-smooth and smooth boundary conditions.

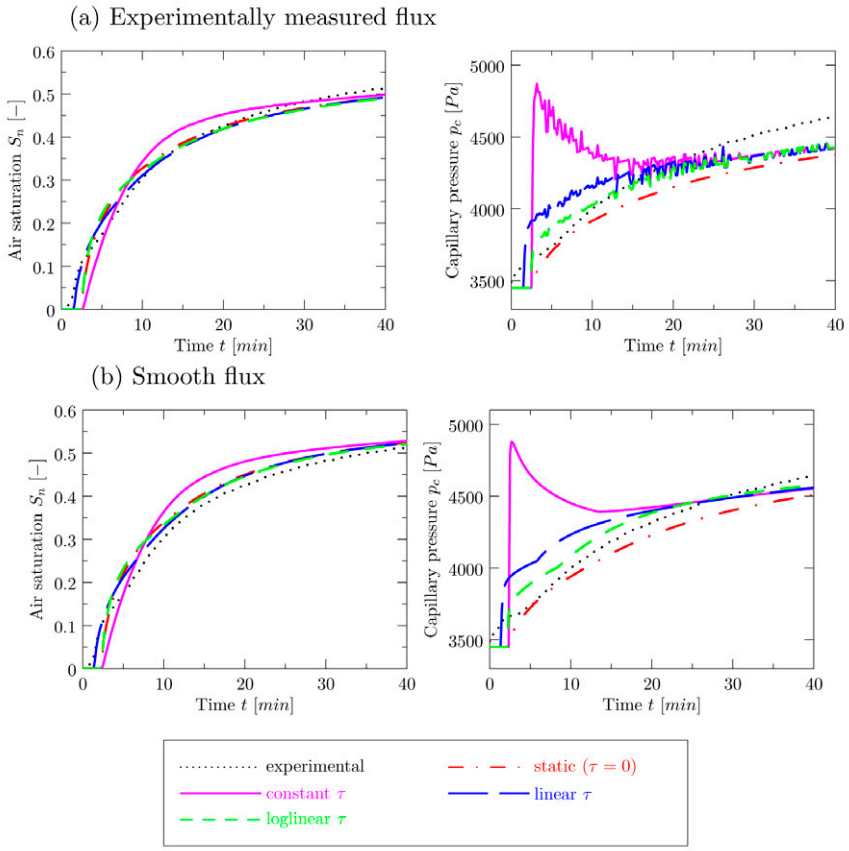

Fig. 9. Numerical solutions obtained with (a) laboratory-measured flux u_{water} (solid line in Fig. 8) and (b) smooth flux u^*_{water} (dashed line in Fig. 8) for Case 1 in Fig. 6 compared with the measured laboratory values of air saturation S_n and capillary pressure p_c in the middle of the column for various models of the dynamic coefficient $\tau = \tau(S_w)$, where S_w is the wetting-phase saturation. The temporal profiles of the capillary pressure in (a) obtained with measured flux u_{water} resemble those in (b) obtained with smooth flux u^*_{water} (Simulation 1).

static capillary pressure. The constant model of $\tau = \tau(S_w)$ exhibited a different behavior in different situations. In Fig. 10a and 10c, for instance, the solution obtained with constant τ has a substantially slower front propagation than other solutions. We believe that this

Table 6. Parameters of the simulation of a fictitious laboratory experiment with a heterogeneous porous medium (Simulations 2 and 3).

Parameter	Value
Initial condition	$S_n(x,0) = 0$ for x in $(0,L)$
Boundary conditions	$u_w(0,t) = 0$ for t in $[0,T]$
	$p_n(0,t) =$ constant $= 0$ for t in $[0,T]$
	$u_w(L,t) = u_{water}{}^*(t)$ for t in $[0,T]$
	$u_n(L,t) = 0$ for t in $[0,T]$
Problem setup	$T = 1500$ s, $L = 10$ cm, $g = 9.81$ m s^{-2}
Capillary pressure	Dynamic capillary pressure p_c, various models for $\tau(S_w)$, Table 1
Materials	Sand A (coarse), Table 1
	Sand B (finer than Sand A), Table 1
	Sand C (finer than Sand A), Table 1
Fluids	Air and water, Table 1

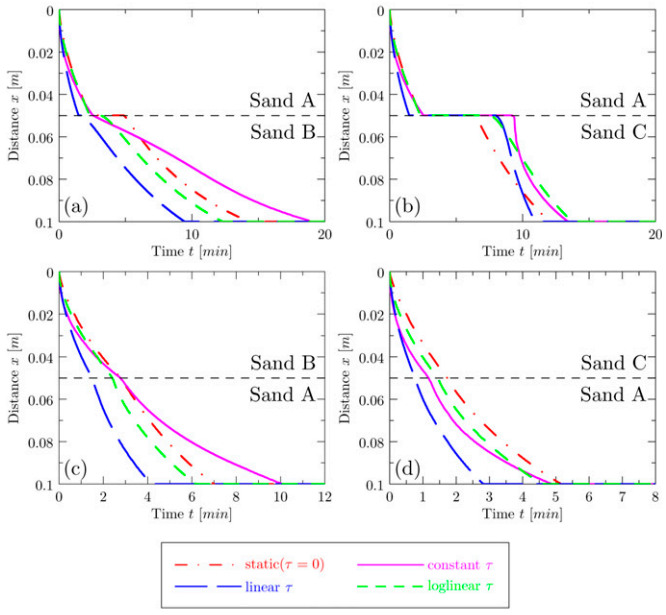

Fig. 10. Position of the air front in time for various models of the dynamic coefficient τ for the layered configurations of porous media shown in Fig. 6: (a and b) Case 2 and (c and d) Case 3. Note that both Sands B and C are finer than Sand A and, therefore, (a) and (b) show situations where the barrier effect is simulated (Simulation 2).

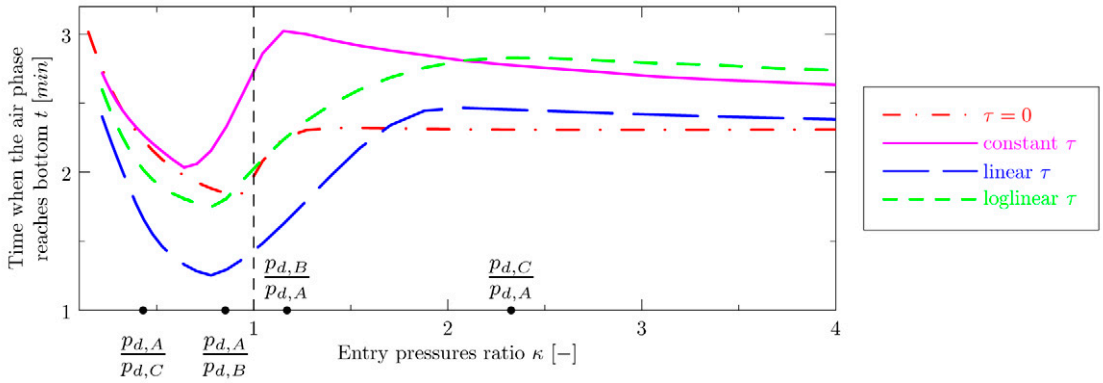

Fig. 11. The time at which the air phase reaches the lower boundary for various models of the dynamic coefficient τ for the case of the layered configuration of porous media shown in Fig. 6 (Case 4) for multiple choices of the ratio $\kappa = p_{\mathrm{d},A_\kappa} / p_{\mathrm{d,A}}$, where p_{d,A_κ} and $p_{\mathrm{d,A}}$ are the entry pressures of Sand A^κ and Sand A, respectively (Simulation 3).

is because the constant model overestimates the dynamic coefficient for high wetting-phase saturation S_w (see Fig. 7).

The delay of the nonwetting phase at the interface due to the barrier effect differed when various configurations of sands were used. In the case of Sand B with a lower entry pressure than Sand C (Fig. 10a), the time required to penetrate the finer medium was generally smaller when using the dynamic models of capillarity than in the case of static capillary pressure. In the case of the finer Sand C, however, these penetration times were comparable or even larger than in the static case (Fig. 10b).

Simulation 3: Influence of Entry Pressure on Penetration Time of Air under Dynamic Conditions

We used a layered medium configuration, sketched in Fig. 6 (Case 4), to investigate the sensitivity of the propagation speed to the ratio between the entry pressures of layers consisting of Sand A overlying Sand A^κ. The value of the entry pressure in Sand A^κ is defined as $p^\kappa_{\mathrm{d,A}} = \kappa p_{\mathrm{d,A}}$, where $p_{\mathrm{d,A}}$ denotes the entry pressure of Sand A. The intrinsic permeability K_{A_κ} was evaluated using the Leverett scaling $p_c \propto \sqrt{(\Phi/K)}$ (Leverett, 1941) as $K_{A_\kappa} = \kappa^{-2} K_A$, where K_A is the intrinsic permeability of Sand A. We assumed that the porosities of both sands were the same. Unlike in the previous case, we prescribed a constant flow rate $u_w(L,t) = 10^{-4}$ m s^{-1} at the lower boundary of the column. Figure 11 shows the times when the air phase reached the bottom boundary (at x = 10 cm) using the dynamic or static models of capillary pressure. As shown by the long-dashed line in Fig. 11, the propagation speed of the linear model of τ was almost two times faster than in the case of static capillary pressure (dash-dotted line, $\tau = 0$) when the medium was homogeneous ($\kappa = 1$). Then, by increasing κ (i.e., coarse top, fine bottom), the traveling time of the air front for the linear model of $\tau = \tau(S_w)$ increased, and approximately at $\kappa \sim 1.7$, it crosses the curve corresponding to the static capillary pressure. In the case of the log-linear model, the traveling times were similar to the static case when κ was near 1 and they became larger for $\kappa > 1.3$. The constant model had a substantially slower propagation speed with respect to the static case for all considered values of $\kappa > 1$. These results agree with the findings shown in Fig. 10, where the ratio between the entry pressures is $\kappa_{A/B} = 1.17$

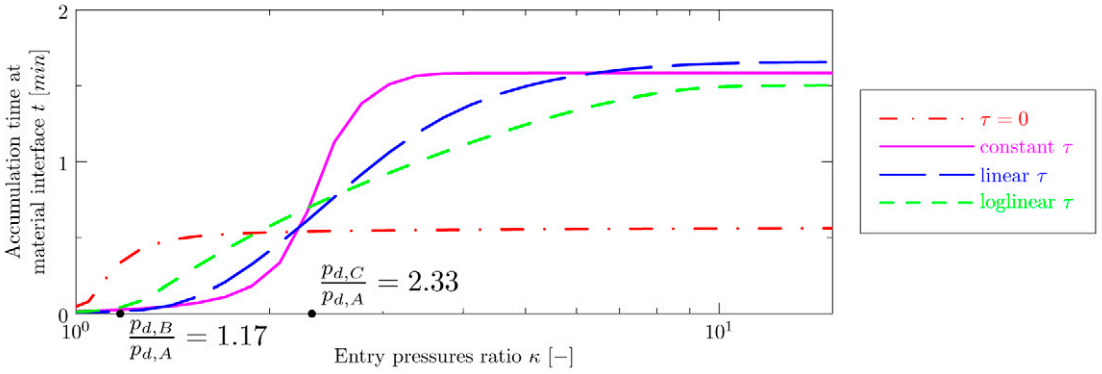

Fig. 12. Accumulation time of the air phase at the material interface (i.e., delay of the air at the interface due to the capillary barrier effect) for various models of the dynamic coefficient τ for the case of the layered configuration of porous media shown in Fig. 6 (Case 4) for multiple choices of the ratio $\kappa = p_{\mathrm{d},A_\kappa} / p_{\mathrm{d,A}}$, where p_{d,A_κ} and $p_{\mathrm{d,A}}$ are the entry pressures of Sand A^κ and Sand A, respectively. The interface was placed at x = 5 cm (Simulation 3).

and $\kappa_{A/C} = 2.33$ for the Sand A over Sand B and Sand A over Sand C configurations, respectively.

To explain different delays at the interface observed in Simulation 2 (Fig. 10a and 10b), we focused on the situations where the barrier effect was simulated, i.e., $\kappa > 1$. In Fig. 12, we plotted accumulation times as a function of κ. Here, the accumulation time is defined as the delay between the times when the nonwetting phase reached and when it penetrated the material interface. In Fig. 12, the results approximately correspond to the already observed behavior of different simulated delays due to the barrier effect in Fig. 10a and 10b (see the points $p_{d,B}/p_{d,A}$ and $p_{d,C}/p_{d,A}$ in Fig. 12). In general, the accumulation times for $\kappa < 2$ are notably lower and for $\kappa > 3$ substantially higher when using the dynamic effect in capillarity compared with the referential curve with static capillary pressure (drawn as a dash-dotted line). Additionally, for higher differences in entry pressures, the curves tended to steady and when using the model of capillarity with dynamic effect, the accumulation times were more than three times higher than in the case of static capillary pressure. Hence, in the case of a heterogeneous medium, the inclusion of the dynamic effect in the capillary pressure may substantially change the simulated evolution of the flow because the entry pressure of the finer porous medium can be achieved sooner or later than in the static case (see Fig. 10 and 11).

Conclusions

A one-dimensional numerical scheme of two-phase incompressible and immiscible flow is presented that enables simulation of two-phase flow in both homogeneous and heterogeneous media under dynamic capillary pressure conditions where the treatment of the conditions at the material interfaces is not numerically trivial. The numerical scheme was verified and its order of convergence was estimated using semianalytical solutions for homogeneous and heterogeneous porous media, respectively.

Laboratory-measured parameters were used in the numerical simulation of the dynamic capillary pressure including three models of the dynamic effect coefficient $\tau = \tau(S_w)$. The numerical solutions for the dynamic effect in the capillary pressure showed that the dynamic effect has a significant impact on the magnitude of the capillary pressure, while the change in the saturation profiles may be considered negligible in some cases. The constant model of τ showed a rather unrealistic profile of the numerical approximation of the capillary pressure when compared with the laboratory-measured data.

The results of the simulation indicate that the dynamic effect may not be so important in drainage problems in a homogeneous porous medium, but it is of great importance in heterogeneous media where the capillarity governs flow across the material interfaces. The linear model of τ accelerated the flow of air across the interface for both configurations of the coarse and fine porous media when the ratio between entry pressures of the media was close to 1. In all other cases, the use of the dynamic effect seemed to increase the time needed for the nonwetting fluid to accumulate at a finer sand interface (a delay due to the barrier effect). This suggests that without dynamic effects, the travel time of the nonwetting phase can possibly be estimated to be smaller or larger than the actual time. The conclusion can be settled by laboratory experiment only.

The methodology used in this study is currently being developed for the two-dimensional case. Two-dimensional laboratory experiments are also in preparation.

Appendix

List of Symbols

α index of wetting (w) or nonwetting (n) fluid
α_S scaling parameter in Stauffer model τ_S
ε order of convergence of a numerical scheme
κ ratio between entry pressures
λ Brooks–Corey pore size distribution index
μ dynamic viscosity, kg m^{-1} s^{-1}
$\mathbf{n}$ outer normal unit vector
Φ porosity
ρ density, kg m^{-3}
τ dynamic effect coefficient, kg m^{-1} s^{-1}
τ_S Stauffer model of dynamic effect coefficient, kg m^{-1} s^{-1}
Ω Computational domain
Γ Boundary of Ω
Γ^D Dirichlet-type boundary subset of Γ
Γ^N Neumann-type boundary subset of Γ
g gravitational acceleration, m s^{-2}
K intrinsic permeability, m^2
k_r relative permeability
L length of the domain, m
p pressure, kg m^{-1} s^{-2}
p_c capillary pressure, kg m^{-1} s^{-2}
p_c^{eq} static capillary pressure, kg m^{-1} s^{-2}
p_d Brooks–Corey entry pressure, kg m^{-1} s^{-2}
S saturation
S_r residual saturation
S^e effective saturation
T final time of the simulation, s
u fluid velocity, m s^{-1}

Acknowledgments

This work has been supported by the project "Applied Mathematics in Technical and Physical Sciences" MSM 6840770010, Ministry of Education of the Czech Republic; the project "Environmental modeling" KONTAKT ME878, Ministry of Education of the Czech Republic; the National Science Foundation through the award 0222286 (CMG Research: "Numerical and Experimental Validation of Stochastic Upscaling for Subsurface Contamination Problems Involving Multiphase Volatile Chlorinated Solvents"); and the project "Mathematical Modelling of Multiphase Porous Media Flow" 201/08/P567 of the Czech Science Foundation (GA ČR).

References

Bastian, P. 1999. Numerical computation of multiphase flows in porous media. Habilitation thesis. Kiel Univ., Kiel, Germany.

Bear, J., and A. Verruijt. 1990. Modeling groundwater flow and pollution. D. Reidel, Dordrecht, the Netherlands.

Brooks, R.H., and A.T. Corey. 1964. Hydraulic properties of porous media. Hydrol. Pap. 3. Colorado State Univ., Fort Collins.

Burdine, N.T. 1953. Relative permeability calculations from pore-size distribution data. Trans. Am. Inst. Min. Eng. 198:71–78.

Camps-Roach, G., D.M. O'Carroll, T.A. Newson, T. Sakaki, and T.H. Illangasekare. 2010. Experimental investigation of dynamic effects in capillary pressure: Grain size dependency and upscaling. Water Resour. Res. (in press), doi:10.1029/2009WR008792.

Dahle, H.K., M.A. Celia, and M.S. Hassanizadeh. 2005. Bundle-of-tubes model for calculating dynamic effects in the capillary-pressure–saturation relationship. Transp. Porous Media 58:5–22.

de Neef, M.I., and J. Molenaar. 1997. Analysis of DNAPL Infiltration in a medium with a low-permeable lens. Comput. Geosci. 1:191–214.

Fučík, R., M. Beneš, J. Mikyška, and T.H. Illangasekare. 2004. Generalization of the benchmark solution for the two-phase porous-media flow. p. 181–184. *In* K. Kovar et al. (ed.) Int. Conf. on Finite-Element Models, MODFLOW, and More: Solving Groundwater Problems, Carlsbad, Czech Republic. 13–16 Sept. 2004.

Fučík, R., J. Mikyška, and T.H. Illangasekare. 2005. Evaluation of saturation-dependent flux on two-phase flow using generalized semi-analytic solution. p. 23–35. *In* M. Beneš et al. (ed.) Proc. Czech–Japanese Seminar in Applied Mathematics. Faculty of Nucl. Sci. and Phys. Eng., Czech Tech. Univ., Prague.

Fučík, R., J. Mikyška, M. Beneš, and T.H. Illangasekare. 2007. An improved semi-analytical solution for verification of numerical models of two-phase flow in porous media. Vadose Zone J. 6:93–104.

Fučík, R., J. Mikyška, M. Beneš, and T.H. Illangasekare. 2008. Semianalytical solution for two-phase flow in porous media with a discontinuity. Vadose Zone J. 7:1001–1007.

Fučík, R., J. Mikyška, T. Sakaki, and T.H. Illangasekare. 2009. Numerical study of the effect of dynamic capillary pressure in porous medium. p. 14–30. *In* M. Beneš et al. (ed.) Proc. Czech–Japanese Seminar in Applied Mathematics 2008. COE Lecture Note, Vol. 14. Faculty of Math., Kyushu Univ., Fukuoka, Japan.

Gray, W.G., and S.M. Hassanizadeh. 1991a. Paradoxes and realities in unsaturated flow theory. Water Resour. Res. 27:1847–1854.

Gray, W.G., and S.M. Hassanizadeh. 1991b. Unsaturated flow theory including interfacial phenomena. Water Resour. Res. 27:1855–1863.

Hassanizadeh, S.M., M.A. Celia, and H.K. Dahle. 2002. Dynamic effect in the capillary pressure–saturation relationship and its impacts on unsaturated flow. Vadose Zone J. 1:38–57.

Hassanizadeh, S.M., and W.G. Gray. 1993. Thermodynamic basis of capillary pressure in porous media. Water Resour. Res. 29:3389–3406.

Helmig, R. 1997. Multiphase flow and transport processes in the subsurface: A contribution to the modeling of hydrosystems. Springer-Verlag, Berlin.

Helmig, R., A. Weiss, and B.I. Wohlmuth. 2007. Dynamic capillary effects in heterogeneous porous media. Comput. Geosci. 11:261–274.

Helmig, R., A. Weiss, and B.I. Wohlmuth. 2009. Variational inequalities for modeling flow in heterogeneous porous media with entry pressure. Comput. Geosci. 13:1–17.

Illangasekare, T.H., E.J. Armbruster III, and D.N. Yates. 1995. Non-aqueous-phase fluids in heterogeneous aquifers: Experimental study. J. Environ. Eng. 121:571–579.

Ippisch, O., H.J. Vogel, and P. Bastian. 2006. Validity limits for the van Genuchten–Mualem model and implications for parameter estimation and numerical simulation. Adv. Water Resour. 29:1780–1789.

LeVeque, R.J. 2002. Finite volume methods for hyperbolic problems. Cambridge Univ. Press, Cambridge, UK.

Leverett, M.C. 1941. Capillary behavior in porous solids. Trans. Am. Inst. Min. Eng. 142:152–169.

Manthey, S. 2006. Two-phase flow processes with dynamic effects in porous media: Parameter estimation and simulation. Inst. für Wasserbau der Universität Stuttgart, Stuttgart, Germany.

Manthey, S., M.S. Hassanizadeh, and R. Helmig. 2005. Macro-scale dynamic effects in homogeneous and heterogeneous porous media. Transp. Porous Media 58:121–145.

McWhorter, D.B., and D.K. Sunada. 1990. Exact integral solutions for two-phase flow. Water Resour. Res. 26:399–413.

Mikyška, J., M. Beneš, and T.H. Illangasekare. 2009. Numerical investigation of non-aqueous phase liquid behavior at heterogeneous sand layers using VODA multiphase flow code. J. Porous Media 12:685–694.

Nieber, J.L., R.Z. Dautov, A.G. Egorov, and A.Y. Sheshukov. 2005. Dynamic capillary pressure mechanism for instability in gravity-driven flows: Review and extension to very dry conditions. Transp. Porous Media 58:147–172.

Nordbotten, J.M., M.A. Celia, H.K. Dahle, and S.M. Hassanizadeh. 2007. Interpretation of macroscale variables in Darcy's law. Water Resour. Res. 43:W08430, doi:10.1029/2006WR005018.

Nordbotten, J.M., M.A. Celia, H.K. Dahle, and S.M. Hassanizadeh. 2008. On the definition of macroscale pressure for multiphase flow in porous media. Water Resour. Res. 44:W06S02, doi:10.1029/2006WR005715.

O'Carroll, D.M., T.J. Phelan, and L.M. Abriola. 2005. Exploring dynamic effects in capillary pressure in multistep outflow experiments. Water Resour. Res. 41:W11419, doi:10.1029/2005WR004010.

Peszyńska, M., and S.Y. Yi. 2008. Numerical methods for unsaturated flow with dynamic capillary pressure in heterogeneous porous media. Int. J. Numer. Anal. Model. 5:126–149.

Sakaki, T., D.M. O'Carroll, and T.H. Illangasekare. 2010. Direct quantification of dynamic effects in capillary pressure for drainage and wetting cycles. Vadose Zone J. 9:424–437.

Stauffer, F. 1978. Time dependence of the relations between capillary pressure, water content and conductivity during drainage of porous media. p. 3.35–3.52. *In* IAHR Symp. on Scale Effects in Porous Media, Thessaloniki, Greece. 28 Aug.–1 Sept. 1978. Int. Assoc. Hydro-Environ. Eng. Res., Madrid.

van Duijn, C.J., and M.J. de Neef. 1998. Self-similar profiles for capillary diffusion driven flow in heterogeneous porous media. Adv. Water Resour. 21:451–461.

van Duijn, C.J., J. Molenaar, and M.J. de Neef. 1995. The effect of capillary forces on immiscible two-phase flow in heterogeneous porous media. Transp. Porous Media 21:71–93.

van Duijn, C.J., L.A. Peletier, and I.S. Pop. 2007. A new class of entropy solutions of the Buckley–Leverett equation. SIAM J. Math. Anal. 39:507–536.

van Genuchten, M.Th. 1980. A closed-form equation for predicting the hydraulic conductivity of unsaturated soils. Soil Sci. Soc. Am. J. 44:892–898.